Insights into the pion production mechanism and the symmetry energy at high density

Yangyang Liu [1], Yongjia Wang [2], Ying Cui [1], Cheng-Jun Xia [3], Zhuxia Li [1], Yongjing Chen [1], Qingfeng Li [2,4,*] and Yingxun Zhang [1,5,†]

[1] *China Institute of Atomic Energy, Beijing 102413, China*
[2] *School of Science, Huzhou University, Huzhou 313000, China*
[3] *School of Information Science and Engineering, Zhejiang University Ningbo Institute of Technology, Ningbo 315100, China*
[4] *Institute of Modern Physics, Chinese Academy of Sciences, Lanzhou 730000, China*
[5] *Guangxi Key Laboratory of Nuclear Physics and Technology, Guangxi Normal University, Guilin 541004, China*

(Received 16 March 2020; revised 24 June 2020; accepted 7 January 2021; published 29 January 2021)

The pion production mechanism is explored based on the ultrarelativistic quantum molecular dynamics model (UrQMD) in which the Δ-mass dependence of the $\mathcal{M}$ matrix and Δ-mass dependence of the momentum $p_{N\Delta}$ in $N\Delta \to NN$ cross sections are taken into account. By analyzing the time evolution of the pion production rate and the density in the overlapped region for the reaction of Au+Au at the beam energy of 0.4A GeV, we find that characteristic density of pion observable is in the region of 1–2 times normal density. The process of pion production in the reaction is tracked, including the loops of $NN \leftrightarrow N\Delta$ and $\Delta \leftrightarrow N\pi$, and our calculations show that the sensitivity of π^-/π^+ to symmetry energy is weakened after 4–5 N-Δ-π loops in the pion production path. The π^-/π^+ ratio in the reaction near the threshold energies retains its sensitivity to the symmetry energy, and it is insensitive to the nuclear incompressibility K_0 and effective mass when their values are selected in the commonly accepted range. By comparing the UrQMD calculations to the FOPI data at 0.4A GeV and considering the constraint of symmetry energy from neutron star properties, the slope of symmetry energy $L = 54$–91 MeV and the symmetry energy at two times normal density $S(2\rho_0) = 48$–59 MeV are deduced, and they are also consistent with the constraint from the ASY-EOS flow data.

DOI: 10.1103/PhysRevC.103.014616

I. INTRODUCTION

The isospin asymmetric nuclear equation of state is very important for understanding both nuclear physics and astrophysics. Recently, the values of neutron star masses, radii, and tidal deformability obtained from the binary neutron star merging event GW170817 attracted lots of analyses of their favored nucleonic equation of state at suprasaturation density [1–10] and the inferred symmetry energy at two times normal density is 39–53 MeV [7,8,11]. In the laboratory, the intermediate energy heavy ion collisions (HICs) can also provide the constraints of symmetry energy around twice the saturation density by using the pion production ratios, and it has become an important goal of nuclear scientific research [10,12,13].

The pions are mainly produced through Δ resonance decay in intermediate energy HICs; thus, the ratio of pion's multiplicity, i.e., $M(\pi^-)/M(\pi^+)$ (simply named the π^-/π^+ ratio), was supposed as a probe to constrain the symmetry energy at suprasaturation density [14,15]. In 2007, FOPI published the pion data, such as $M(\pi)$ and π^-/π^+ [16], at the beam energies ranging from 0.4A to 1.5A GeV. Many theoretical calculations have been performed to extract the symmetry energy by best fitting the FOPI data of $M(\pi)$ and π^-/π^+. Those calculations clearly show that the π^-/π^+ ratio near the threshold energy is sensitive to the density dependence of the symmetry energy, but different conclusions on the constraint of density dependence of the symmetry energy at suprasaturation density have been made [17–20]. This has inspired both theoretical and experimental studies to deeply understand the pion production mechanism. In the experimental study, the remeasurement of subthreshold pion production at Michigan State University (MSU) and RIKEN for Sn+Sn at the beam energy of 270A MeV has been performed [21]. On the theoretical side, the influences of the threshold effect of $NN \leftrightarrow N\Delta$ [20,22], pion potential [23–28], Δ potential [29,30], cluster formation [31], Pauli blocking [32], and energy conservation issue [30,33] were investigated individually to deeply understand the pion production mechanism. The calculations show that including the different physics in transport models could influence the prediction of π^-/π^+ [26].

On the other hand, the model dependence should be well understood. Code comparison projects have been inspired in the past 20 years [34–37] to improve the reliability of transport models. Recently, the results of code comparison by Akira *et al.* [37] found that a better method for treating the baryon production and decay in the collision part of transport models is to adopt the time-step-free method, which automatically determines the order of two-body collision or resonance decay according to their collision time and decay time. This method has been adopted in many codes, such as UrQMD [38–40], Jet AA Microscopic transport model (JAM) [31,41], and Simulating Many Accelerated Strongly interacting Hadrons

*liqf@zjhu.edu.cn
†zhyx@ciae.ac.cn

(SMASH) [42]. Since the UrQMD model has been well designed for solving the particle's production and decay in the collision part of the transport equation, we decide to adopt it to investigate the pion production mechanism near the threshold energy by analyzing the time evolution of pion production rate and the loop of $N \leftrightarrow \Delta \leftrightarrow \pi$, and the constraint of symmetry energy at 1–2ρ_0.

This paper is organized as follows: In Sec. II, we first briefly introduce the UrQMD model and then describe the interaction parameters and the cross sections we used. Considering the Δ-mass dependent cross sections of the channel of $N\Delta \to NN$ which is obtained based on the one-boson exchange model in the UrQMD model, we investigate the effect of $N\Delta \to NN$ on the $M(\pi)$ and π^-/π^+ near the threshold energy. In Sec. III, we investigate the pion production mechanism and characteristic density of the pion observable. The influences of symmetry energy, incompressibility, effective mass, and symmetry potential of Δ on pion observables are discussed with the UrQMD model. The symmetry energy constraints from π^-/π^+ ratios, the tidal deformability, and the maximum mass of neutron star are finally obtained. The summary and outlook are given in Sec. IV.

II. URQMD MODEL AND $N\Delta \to NN$ CROSS SECTIONS

The UrQMD model is a microscopic many-body approach to simulate the reaction of *p*-*p*, *p*-*A*, and *A*-*A* systems in the large energy range from SIS to the Large Hadron Collider (LHC). It consists mainly of the initialization of projectile and target nuclei, the mean field, and the collision term [38].

In the UrQMD model, hadrons are represented by Gaussian wave packets with the width parameter σ_r. After the initialization of projectile and target nuclei, the time evolution of the coordinate and momentum of hadron i is propagated according to the Hamilton equations of motion:

$$\dot{\vec{r}}_i = \frac{\partial H}{\partial \vec{p}_i}, \quad \dot{\vec{p}}_i = -\frac{\partial H}{\partial \vec{r}_i}. \tag{1}$$

The Hamiltonian H contains the kinetic energy and the effective interaction potential energy U [43].

The form of the isocalar part of potential energy density used in this work is

$$u = \frac{\alpha}{2}\frac{\rho^2}{\rho_0} + \frac{\beta}{\eta+1}\frac{\rho^{\eta+1}}{\rho_0^{\eta}} + \frac{g_{\rm sur}}{2\rho_0}(\nabla\rho)^2 + \frac{g_{\rm sur,iso}}{\rho_0}[\nabla(\rho_n-\rho_p)]^2 + u_{md}. \tag{2}$$

The energy density related to the momentum-dependent interaction is obtained based on the isospin-independent momentum-dependent interaction as in Ref. [44], i.e., $t_4 \ln^2(1+t_5(\mathbf{p}_1-\mathbf{p}_2)^2)\delta(\mathbf{r}_1-\mathbf{r}_2)$, and it yields the effective mass $m^*/m = (1+\frac{m}{p}\frac{dU}{dp})^{-1} = 0.77$ at Fermi momentum. The parameter set used in this work is an updated SM EOS with $K_0 = 231$ MeV, as in Table I, which is in the commonly accepted region $K_0 = 220 \pm 40$ MeV determined by the nucleonic flow [45] and giant monopole resonance (GMR) [46]. To see the effects of different K_0 on the pion observable and neutron star, we also did the calculations with Soft EOS with momentum dependent interaction (SM EOS) with $K_0 =$ 200 MeV as in Ref. [47] and a simple discussion is given in Secs. III C and III D.

TABLE I. Parameters in UrQMD. α, β are in MeV, and $g_{\rm sur}$ and $g_{\rm sur,iso}$ are in MeV fm^2. t_4 and t_5 are the coefficients in momentum-dependent interaction, in MeV and MeV^{-2}, and $\rho_0 = 0.16$ fm^{-3}. Last two columns are K_0 in MeV and m^*/m. The width of Gaussian wave packet is taken as 1.414 fm for Au+Au.

α	β	η	$g_{\rm sur}$	$g_{\rm sur,iso}$	t_4	t_5	K_0	m^*/m
−221	153	1.31	19.5	−11.3	1.57	5×10^{-4}	231	0.77

For the isovector part of potential energy, the Skyrme-type polynomial form [form (a) in Eq. (3)] and the density power law form [form (b) in Eq. (3)] are adopted. It reads

$$u_{\rm sym} = S^{pot}_{\rm sym}(\rho)\rho\delta^2 = \begin{cases} (A(\frac{\rho}{\rho_0}) + B(\frac{\rho}{\rho_0})^{\gamma_s} + C(\frac{\rho}{\rho_0})^{5/3})\rho\delta^2, & \text{(a)} \\ \frac{C_s}{2}(\frac{\rho}{\rho_0})^{\gamma_i}\rho\delta^2. & \text{(b)} \end{cases}. \tag{3}$$

The parameters of Eq. (3) used in this work are listed in Table II, which correspond to five different density dependences of symmetry energy. The last three columns in Table II are the corresponding values of symmetry energy coefficient $S_0 = S(\rho_0)$, the slope $L = 3\rho_0(\frac{\partial S(\rho)}{\partial\rho})|_{\rho=\rho_0}$, and symmetry energy at $2\rho_0$, i.e., $S(2\rho_0)$. Here, $S(\rho) = \frac{\hbar^2}{6m}(\frac{3\pi^2\rho}{2})^{2/3} + S^{pot}_{\rm sym}(\rho)$.

The symmetry potential of Δ resonance is calculated from the symmetry potential of nucleon according to

$$\begin{aligned} V^{\Delta^{++}}_{\rm sym} &= V^p_{\rm sym}, \\ V^{\Delta^{+}}_{\rm sym} &= \frac{1}{3}V^n_{\rm sym} + \frac{2}{3}V^p_{\rm sym}, \\ V^{\Delta^{0}}_{\rm sym} &= \frac{2}{3}V^n_{\rm sym} + \frac{1}{3}V^p_{\rm sym}, \\ V^{\Delta^{-}}_{\rm sym} &= V^n_{\rm sym}, \end{aligned} \tag{4}$$

which is the same as those used in Refs. [15,19,20,22,30,39]. The threshold effect and the pion optical potential have been studied with various models but still with some puzzling inconsistencies [23–26]. Further studies are certainly required [27]. For simplicity, we will not consider the threshold effect in the present work, since introducing this effect needs to largely improve the collision treatments in UrQMD. We plan to study it in the near future.

TABLE II. Parameters of symmetry potential in UrQMD. A, B, C, C_s, S_0, $S(2\rho_0)$, and L are in MeV, and γ_s and γ_i are dimensionless.

$\mathbf{S}(\rho)_\mathbf{a}$	A	B	C	γ_s	S_0	L	$S(2\rho_0)$
S_1	62.84	−38.30	−6.39	1.1667	30.	46	38.0
S_2	20.37	10.75	−9.28	1.3	34.	81	57.3
S_3	22.16	−14.3	13.8	1.25	33.	104	73.5
$\mathbf{S}(\rho)_\mathbf{b}$	$\frac{C_s}{2}$	γ_i			S_0	L	$S(2\rho_0)$
G_{05}	20	0.5			32.5	54	47.7
G_{20}	20	2.0			32.5	144	99.5

In the collision term, the medium modified nucleon-nucleon elastic cross sections are the same as those in our previous works [45]. For the $NN \rightarrow N\Delta$ cross sections and decay width of Δ, we use the standard values of UrQMD, where the cross sections of $NN \rightarrow N\Delta$ are obtained by fitting the Conseil Européenn pour la Recherche Nucléaire (CERN) experimental data [38,48] and decay widths depend on the mass of excited resonance [38].

Concerning the $N\Delta \rightarrow NN$ cross sections, they are usually obtained from the measured cross section of $NN \rightarrow N\Delta$ by using the detailed balance, where the treatment of the Δ-mass dependence is partly considered by using the proposed method in Ref. [49]. Here, we apply the Δ-mass dependent $N\Delta \rightarrow NN$ cross sections which were recently calculated based on the one-boson exchange model (OBEM) [50], i.e., $\sigma^{\mathrm{OBEM}}_{N\Delta\rightarrow NN}(\sqrt{s}, m_\Delta)$. At the given value of m_Δ, it is calculated as

$$\sigma^{\mathrm{OBEM}}_{N\Delta\rightarrow NN}(\sqrt{s}, m_\Delta) = \frac{1}{1+\delta_{N_1N_2}}\frac{1}{64\pi^2}\int\frac{|\mathbf{p}'_{12}|}{\sqrt{s_{34}}\sqrt{s_{12}}|\mathbf{p}'_{34}(m_\Delta)|} \times \overline{|\mathcal{M}_{N\Delta(m_\Delta)\rightarrow NN}|^2}d\Omega, \tag{5}$$

$\mathbf{p}'_{34}$ is the momentum of incoming N or Δ, and $\mathbf{p}'_{12}$ is the momentum of outgoing N in center of mass frame. For the $\mathcal{M}$ matrix, there is

$$\overline{|\mathcal{M}_{N\Delta(m_\Delta)\rightarrow NN}|^2} = \frac{(2s_1+1)(2s_2+1)}{(2s_3+1)(2s_4+1)}\overline{|\mathcal{M}(m_\Delta)|^2}, \tag{6}$$

at the same Δ mass for both processes. s_i is the spin of particle i, and $\overline{|\mathcal{M}(m_\Delta)|^2}$ is the $\mathcal{M}$ matrix for $NN \rightarrow N\Delta$. The form of the $\mathcal{M}$ matrix in the calculation of $\sigma^{\mathrm{OBEM}}_{N\Delta\rightarrow NN}(\sqrt{s}, m_\Delta)$ is as same as in Ref. [50], and the parameters in the $\mathcal{M}$ matrix are determined by fitting the experimental data of $pp \rightarrow n\Delta^{++}$ [38,48]. Thus, Δ-mass dependences of $\mathbf{p}'_{34}$ and of the $\mathcal{M}$ matrix in the calculation of cross sections of $N\Delta \rightarrow NN$ by using Eq. (5) are considered simultaneously. The different channels are determined based on the relationship $\sigma_{n\Delta^{++}\rightarrow pp} : \sigma_{p\Delta^{-}\rightarrow nn} : \sigma_{n\Delta^{+}\rightarrow np} : \sigma_{p\Delta^{0}\rightarrow np}: \sigma_{n\Delta^{0}\rightarrow nn} : \sigma_{p\Delta^{+}\rightarrow pp} = 3:3:2:2:1:1$. More details can be found in Ref. [50]. We incorporate the cross sections of $\sigma^{\mathrm{OBEM}}_{N\Delta\rightarrow NN}(\sqrt{s}, m_\Delta)$ directly into the UrQMD model.

In the left panel of Fig. 1, we present the $\sigma_{pp\rightarrow n\Delta^{++}}$ used in the UrQMD [38,48]. In the right panel of Fig. 1, we present $\sigma^{\mathrm{UrQMD}}_{n\Delta^{++}\rightarrow pp}(\sqrt{s})$ (blue line) and $\sigma^{\mathrm{OBEM}}_{n\Delta^{++}\rightarrow pp}(\sqrt{s}, m_\Delta)$ (red lines) at four Δ-mass values, i.e., $m_\Delta = 1.10$, 1.18, 1.232, and 1.387 GeV. Here, $\sigma^{\mathrm{UrQMD}}_{n\Delta^{++}\rightarrow pp}(\sqrt{s})$ is the cross sections used in previous UrQMD model calculations [51], and the cross sections for other channels are determined based on the Clebsch-Gordan relationship. The calculations show that the $\sigma^{\mathrm{OBEM}}_{n\Delta^{++}\rightarrow pp}(\sqrt{s}, m_\Delta)$ is lower than the $\sigma^{\mathrm{UrQMD}}_{n\Delta^{++}\rightarrow pp}(\sqrt{s})$ in low-mass Δ cases, especially around the threshold energy. It means that the hard Δ absorption is too strong when one uses $\sigma^{\mathrm{UrQMD}}_{n\Delta^{++}\rightarrow pp}(\sqrt{s})$, and it results in the underestimation of the pion multiplicity, which has been observed in our previous studies [51] (also can be noticed in Fig. 7 of this paper). We note here that, as overall, the probability for a nucleon to undergo inelastic scattering and to become Δ is less than 10% in HICs around 1A GeV (e.g., see Fig. 4 in the present work and Fig. 2 in Ref. [52]), and thus the influence of $N\Delta \rightarrow NN$ on nucleonic observables is weak.

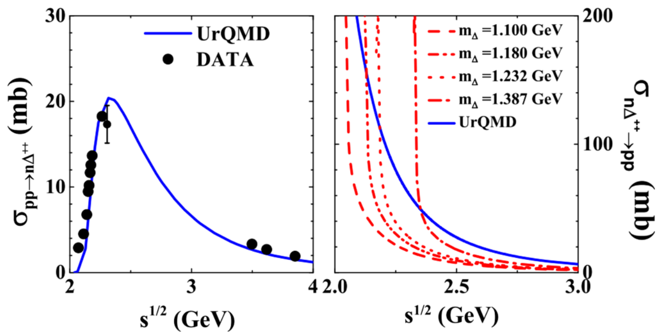

FIG. 1. Left panel: The cross section of $pp \rightarrow n\Delta^{++}$ used in UrQMD; data are taken from Refs. [38,48]. Right panel: The cross sections of $n\Delta^{++} \rightarrow pp$ used in UrQMD and obtained from OBEM model.

III. RESULTS AND DISCUSSION

A. Pion production mechanism

Before drawing the conclusion on the symmetry energy at high density, it is important to investigate the mechanism of the pion production in the UrQMD model by analyzing the time evolution of the density in the compressed region, Δ production, pion production, and the collision and decay number of $NN \leftrightarrow N\Delta$, $N\pi \leftrightarrow \Delta$ for Au+Au at the beam energies from 0.4A to 1.0A GeV.

To obtain an intuitive view of the reaction process, the time evolution of the average density contour plots (upper panels), of the positions of Δ (middle panels), and of the positions of π (bottom panels), for ^{197}Au + ^{197}Au at $b_0 = b/b_{\max} < 0.25$ and $E_{\mathrm{beam}} = 0.4A$ GeV, are presented in Fig. 2. The plots are obtained with 100 events. As shown in the upper panels of Fig. 2, the projectile and target start to touch at a large velocity around 5 fm/c and few Δ resonances appear in the central region. It can be observed in the Fig. 2(b1), where the red points represent the position of Δ. Around 15 fm/c, the density of the compressed system reaches the maximum, and lots of π (violet points) are produced following the Δ production in the compressed region [see Figs. 2(a2), 2(b2), and 2(c2)]. As the time evolves to 25 fm/c, the number of Δ starts to decrease because the Δs decays to nucleon and pion. One can find that the number of π becomes larger with time in the bottom panels of Fig. 2. After 25 fm/c, the system expands to lower densities, and Δs are mainly consumed by the $\Delta \rightarrow N + \pi$ process. The produced πs propagates from high density of the compression phase to low density of the expansion phase, and during the time, πs may experience several $N - \Delta - \pi$ loops before freezing out.

In detail, we present the collision and decay numbers of different channels, such as $N_{\mathrm{coll}}(NN \rightarrow N\Delta)$, $N_{\mathrm{coll}}(N\Delta \rightarrow NN)$, $N_{\mathrm{coll}}(N\pi \rightarrow \Delta)$, and $N_{\mathrm{decay}}(\Delta \rightarrow N\pi)$, as functions of time in Fig. 3. The $N_{\mathrm{coll}}(N\Delta \rightarrow NN)$ is smaller and reaches the maximum about 3 fm/c later in time than $N_{\mathrm{coll}}(NN \rightarrow N\Delta)$. For example, in Au+Au at 0.4A GeV,

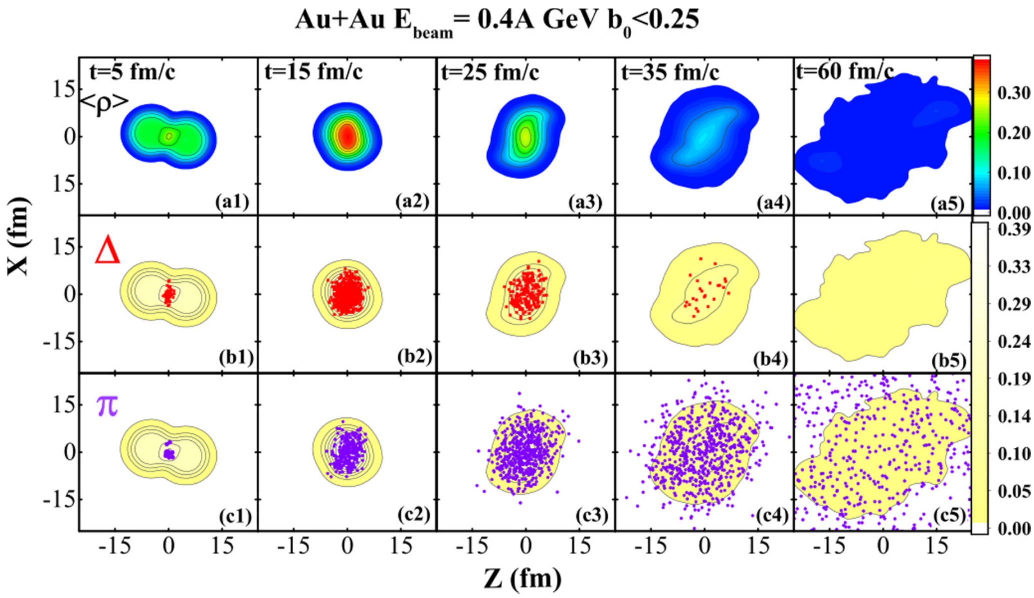

FIG. 2. Panels (a1)–(a5): Snapshots of density contour plots for central collisions ($b_0 < 0.25$), Au+Au reaction at a beam energy of 0.4A GeV. Panels (b1)–(b5) are the positions of Δ resonance (red symbols), and panels (c1)–(c5) are the positions of π mesons (violet symbols). These figures are obtained from 100 events.

the peak of $N_{\rm coll}(NN \rightarrow N\Delta)$ appears around 12.5 fm/c, while $N_{\rm coll}(N\Delta \rightarrow NN)$, $N_{\rm decay}(\Delta \rightarrow N\pi)$, and $N_{\rm coll}(N\pi \rightarrow \Delta)$ peak around 15 fm/c. One important feature is that $N_{\rm decay}(\Delta \rightarrow N\pi)$ and $N_{\rm coll}(N\pi \rightarrow \Delta)$ are higher than $N_{\rm coll}(NN \rightarrow N\Delta)$ and $N_{\rm coll}(N\Delta \rightarrow NN)$ after 15 fm/c. It means the loop of $N\pi \leftrightarrow \Delta$ has a larger possibility than the loop of $NN \leftrightarrow N\Delta$ at a later stage of heavy ion collisions. Also, one can find that the loop of $N\pi \leftrightarrow \Delta$ lasts a long time, i.e., to 35 fm/c, for the beam energies we studied. Our calculations imply that the $M(\pi)$ and π^-/π^- contain the information of symmetry energy at a large region of density variation during the system evolution.

By integrating the collision and decay number over 0–60 fm/c, the probability of different processes in N-Δ-π loops in the UrQMD model are obtained. In Fig. 4, we plot the probabilities of different processes which are similar to the scheme plotted by Bass *et al.* in Ref. [52]. The reaction system is Au+Au at $E_{\rm beam} = 0.4A$ GeV and reduced impact parameter $b_0 < 0.25$. As shown in the scheme, Δ resonances are initially produced via inelastic nucleon nucleon scattering, i.e., $NN \rightarrow N\Delta$, which is also observed from Figs. 2(b1) and 3. For

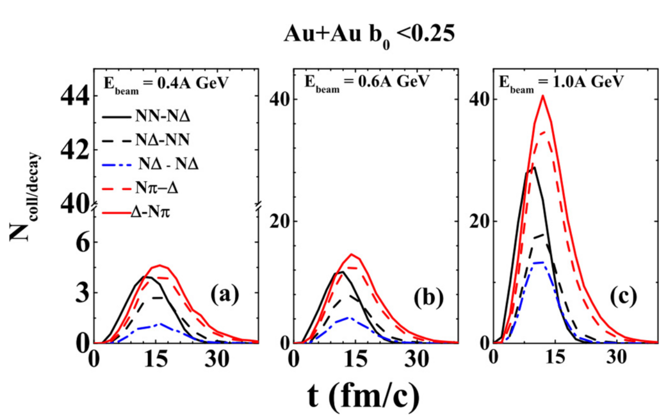

FIG. 3. The number of the Δ-related collision and decay as a function of time at beam energy $E_{\rm beam} = 0.4A$ (a), 0.6A (b), and 1.0A (c) GeV.

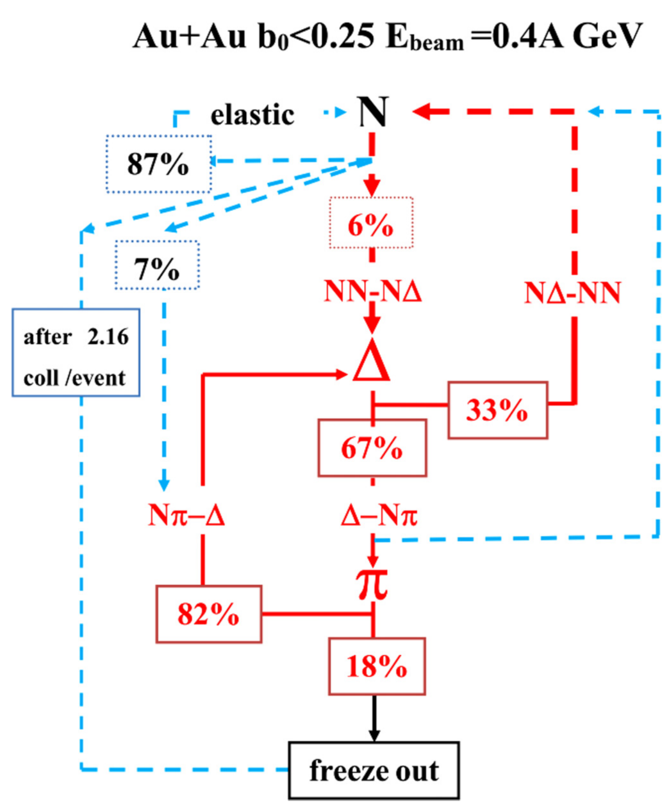

FIG. 4. N-Δ-π loops in the UrQMD model, for Au+Au at $E_{\rm beam} = 0.4A$ GeV and $b_0 < 0.25$ (for more details, see the text).

Au+Au collisions at 0.4A GeV, ≈87% of total NN collisions are elastic collisions, ≈7% belong to $N\pi$ collisions, and ≈6% belong to inelastic collisions of $NN \to N\Delta$. For Δs, there are two kinds of Δ loops: Type (I) is $NN \to N\Delta$ and $N\Delta \to NN$ and type (II) is $\Delta \to N\pi$ and $N\pi \to \Delta$. Qualitatively, one can find that 67% of Δs decay into nucleon and pion, and 33% of them participate in the collision of $\Delta N \to NN$. There are 4.5 N-Δ-π loops before the pion freeze-out, on average. Based on Fig. 3 and the scheme in Fig. 4, one can imagine that the type (I) Δ loop can keep the sensitivity of π^-/π^+ to high-density symmetry energy, but the type (II) Δ loop degrades the sensitivity of π^-/π^+ to high-density symmetry energy.

In reality, both type (I) and type (II) loops reduce the sensitivity of π^-/π^+ to symmetry energy, resulting from the mutual change of the charge state of baryons in the Δ and π production and absorption processes. For example, in the process of $i(n) + j(n) \to i'(p) + j'(\Delta^-)$, a neutron is converted to a proton and may change back to a neutron again during the evolution. For $i(n) + j(n) \to i'(n) + j'(\Delta^0)$, a neutron changes to Δ^0. These processes mean the symmetry potential felt by a neutron may change to the symmetry potential felt by proton or the mixing of neutron and proton symmetry potential as in Eq. (4). The isospin and its third component of the ith particle may change with time, and thus the effects of symmetry energy on nucleons and Δ resonance are weakened, especially at high beam energies where the collision frequencies are large.

B. Characteristic density of pion observable

Considering the complicated process of pion production as discussed above, an important question one has to answer is which density region is eventually probed by $M(\pi)$ and π^-/π^+, and we named this density region the "characteristic density." There were some efforts to answer this question by switching on and off the symmetry energy at different density regions and checking its influence on the pion multiplicity and its ratio [53]. It seems to be a direct way, but the abrupt changes of the symmetry energy in the different density regions could cause unphysical force in the transport model simulations. Thus, it motivates us to extract the characteristic density based on spatiotemporal evolution of pion production.

One method to calculate the characteristic density we propose is to calculate the pion production rate weighted average density during the pion passing time in transport model simulations,

$$\langle \rho_c \rangle_\pi = \frac{\int_{t_0}^{t_1} R_\pi(t)\rho_c(t)dt}{\int_{t_0}^{t_1} R_\pi(t)dt}. \tag{7}$$

The $R_\pi(t) = \frac{dM_\pi(t)}{dt}$ is the pion production rate at a certain time, and $\rho_c(t)$ is an averaged central density, which is calculated in a sphere with a radius equal to 3.35 fm centered at the center of mass of the reaction system. The integral is from $t_0 = 0$ to $t_1 = 60$ fm/c in this work.

In Fig. 5(a), we plot the time evolution of ρ_c/ρ_0 for Au+Au at the beam energy ranging from 0.4A to 1.0A GeV with different colors. As expected, higher beam energy is correlated with larger compressed density, and faster expansion is observed with time evolution. Figure 5(b) shows $R_\pi(t)$ as a function of time. In the beam energy region we studied, the $R_\pi(t)$ reaches its maximum around 15 fm/c. At the beam energy of 0.4A GeV, the system expands to subnormal density after 28 fm/c but pions are continuously produced until ≈40 fm/c. It means that the freeze-out pions are not only from the high density region but also from the low density region at a later stage. The same behaviors can be observed even at the beam energy of 1.0A GeV, which means that the subsequent interactions on the pion production tend to erase the effect of the initial decay that has taken place at high density.

In Fig. 6, the values of $\langle \rho_c/\rho_0 \rangle_\pi$ at all the beam energies we studied are presented and the values are around 1.6ρ_0, which

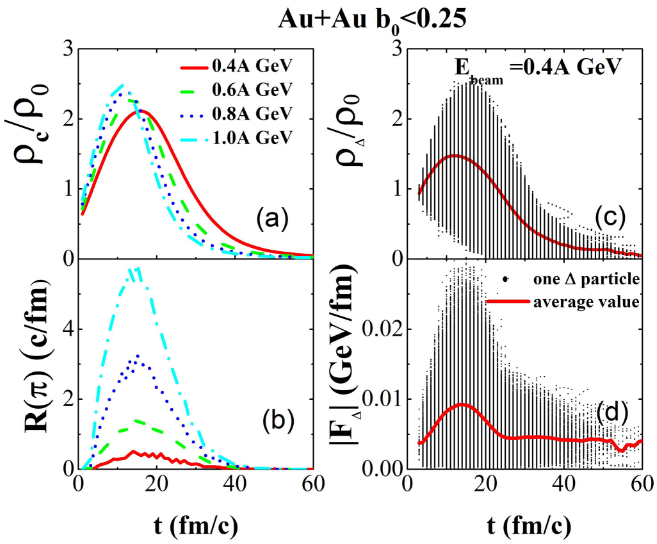

FIG. 5. Time evolution of the averaged density in the center of reaction system (a) and pion production rate (b). Panels (c) and (d) show the density and force of Δ obtained from thousands of events.

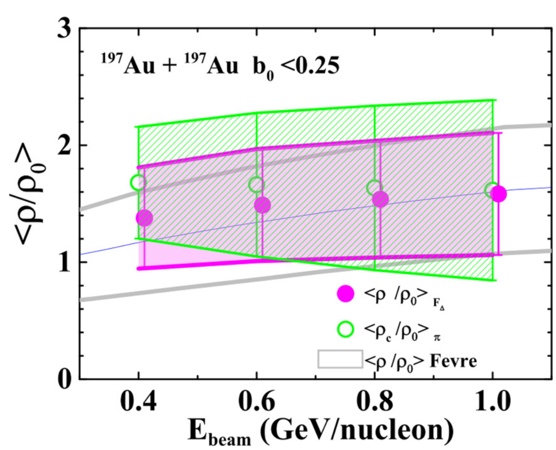

FIG. 6. Pion-weighted density (green open symbols) and the force acting on Δ weighted density (magenta solid symbols) at the beam energy from 0.4–1.0A GeV. The region within gray lines is the characteristic density probed by flow observable [54].

does not increase obviously with the increasing beam energy. This seems contradictory with the impression we have. This is because the system spends a larger fraction of the total time until freeze-out at lower densities for higher beam energy than that for lower beam energy. For example, at the beam energy of 1A GeV, the system takes about 19 fm/c at $\rho_c > \rho_0$ and about 41 fm/c at $\rho_c < \rho_0$, but at the beam energy of 0.4A GeV, the system takes about 26 fm/c at $\rho_c > \rho_0$ and about 34 fm/c at $\rho_c < \rho_0$. Thus, the characteristic density obtained with pion production rate over time becomes almost constant. Due to the above behaviors, the density variance, which is defined as

$$\sigma_\rho^2 = \frac{\int_{t_0}^{t_1} R_\pi(t)(\rho_c(t) - \langle\rho_c\rangle_\pi)^2 dt}{\int_{t_0}^{t_1} R_\pi(t)dt}, \tag{8}$$

increases with the increasing beam energy.

To obtain a comprehensive understanding of the characteristic density related to the pion productions, we also investigate $\rho_\Delta^{(i)}(t)$ and $|F_\Delta^{(i)}(t)|$ as a function of time for Au+Au at 0.4A GeV. The $\rho_\Delta^{(i)}(t)$ and $|F_\Delta^{(i)}(t)|$ are the density where the ith Δ is located and the force acting on ith Δ, respectively, and they are plotted in Figs. 5(c) and 5(d). The black points are the density or force obtained from different events, and one can observe that ρ_Δ distributes from subnormal density to supranormal density even at the stage of the highly compressed phase. It leads to the average values of $\rho_\Delta/\rho_0 \leqslant 1.5$, as illustrated with the red line in Fig. 5(c). Based on $\rho_\Delta^{(i)}$ and $|F_\Delta^{(i)}|$, we calculate the Δ-force weighted density as follows:

$$\langle\rho\rangle_{F_\Delta} = \frac{\int_{t_0}^{t_1} \sum_i |F_\Delta^{(i)}(t)|\rho_\Delta^{(i)}(t)dt}{\int_{t_0}^{t_1} \sum_i |F_\Delta^{(i)}(t)|dt}. \tag{9}$$

The $|F_\Delta|$-weighted average density and its standard deviation are also presented in Fig. 6 with magenta circle symbols and shadows. Our calculations show $|F_\Delta|$-weighted average densities are slightly smaller than those obtained with $R(\pi)$-weighted density and have an increasing trend with the beam energy. It can be understood from Figs. 3 and 5, where the Δs are found to exist for shorter times than pions, and average ρ_Δ is smaller than the average central density of system. Even there is little difference, as both $|F_\Delta|$-weighted average density and R_π-weighted average density methods show that the pion observable carries the information of compressed nuclear matter in the density region of 1–2.5 times normal density, which is larger than the force-weighted characteristic density for the flow observable. The force-weighted characteristic density for flow observable is in 0.7–2.2 times normal density at the beam energy from 0.4A to 1.0A GeV in Ref. [54]. Based on our calculations and the results in Ref. [54], for probing the symmetry energy at the density $>2.5\rho_0$ with HICs, one may need to measure kaon and Σ [22,55–57], or propose new probes.

C. Effects of $\sigma_{N\Delta\to NN}$, incompressibility K_0, and symmetry energy on $M(\pi)$ and π^-/π^+

Now, let us investigate the influence of $\sigma_{N\Delta\to NN}$, incompressibility K_0, and symmetry energy on $M(\pi)$ and π^-/π^+. All simulations are performed with 200 000 events and impact

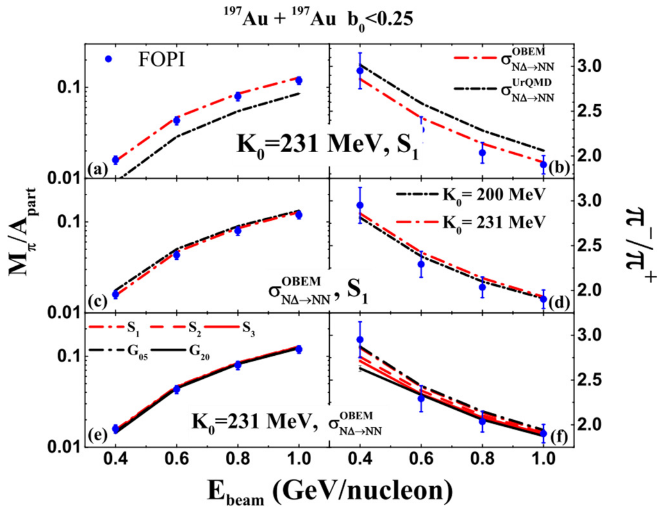

FIG. 7. The excitation function of the $M(\pi)/A_{part}$ (left panels), and π^-/π^+ (right panels), for central collisions of ^{197}Au + ^{197}Au reaction. Panels (a) and (b) are the results with $\sigma_{N\Delta\to NN}^{\rm OBEM}$ (red lines) and $\sigma_{N\Delta\to NN}^{\rm UrQMD}$ (black lines). Panels (c) and (d) are the results with $K_0 = 200$ MeV (black lines) and $K_0 = 231$ MeV (red lines). Panels (e) and (f) are results with different forms of symmetry energy. The FOPI data are shown as solid symbols [16].

parameters range from 0 to 3.35 fm. The upper panels of Fig. 7 are the results of the $M(\pi)/A_{part}$ and π^-/π^+ ratios obtained with two kinds of $N\Delta \to NN$ cross section in the UrQMD calculations in the case of $K_0 = 231$ MeV and symmetry energy with S_1, for Au+Au at beam energy from 0.4A to 1.0A GeV. The black lines are the results obtained with the form of $\sigma_{N\Delta\to NN}^{\rm UrQMD}(\sqrt{s})$ given in the UrQMD [51], where $M(\pi)$ is underestimated as that found in Ref. [51], and the π^-/π^+ ratios are overestimated. The red lines are the results by applying the $\sigma_{N\Delta\to NN}^{\rm OBEM}(\sqrt{s}, m_\Delta)$ [50] in the UrQMD model. With $\sigma_{N\Delta\to NN}^{\rm OBEM}(\sqrt{s}, m_\Delta)$, $M(\pi)$ is enhanced and π^-/π^+ are suppressed. Both $M(\pi)$ and π^-/π^+ ratio are close to the FOPI data, within the experimental uncertainties. The refined descriptions can be understood from Fig. 1, where the values of $\sigma_{N\Delta\to NN}^{\rm OBEM}(\sqrt{s}, m_\Delta)$ are lower than those of $\sigma_{N\Delta\to NN}^{\rm UrQMD}(\sqrt{s})$ for low mass Δ near the threshold energy. As a result, it leads about 67% of the produced Δs, which are produced by the $NN \to N\Delta$ process, entering into the $\Delta \to N\pi$ process, while the probability was only about 51% if the $\sigma_{N\Delta\to NN}^{\rm UrQMD}(\sqrt{s})$ was used in the UrQMD calculations. Thus, the π multiplicities are enhanced and π^-/π^+ ratios are decreased with $\sigma_{N\Delta\to NN}^{\rm OBEM}(\sqrt{s}, m_\Delta)$ compared with those with $\sigma_{N\Delta\to NN}^{\rm UrQMD}$.

Figures 7(c) and 7(d) show the influence of K_0 on $M(\pi)$ and π^-/π^+ with the symmetry energy of S_1 and $\sigma_{N\Delta\to NN}^{\rm OBEM}$ in the UrQMD calculations. The black solid and red dash-dotted lines are the results obtained with $K_0 = 200$ MeV and $K_0 = 231$ MeV, respectively. The calculations show that more pions are produced for the case of $K_0 = 200$ MeV, and the values of $M(\pi)$ are on the upper limits of the data uncertainties, while the π^-/π^+ ratios are reduced by less than 5%. Thus, we can roughly say that the constrained value of L will be not largely influenced by varying K_0 in its generally accepted range, i.e., $K_0 = 220 \pm 40$ MeV.

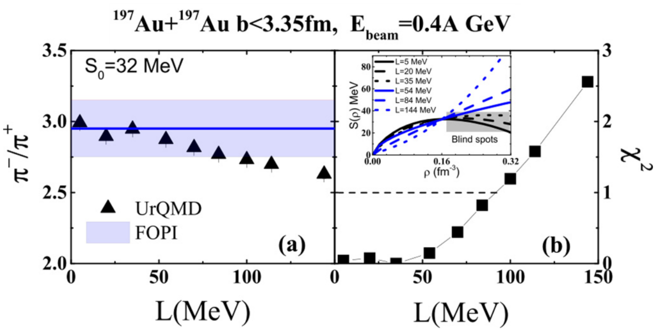

FIG. 8. Panel (a) is for π^-/π^+ as a function of L, and the shaded region are the FOPI data at 0.4A GeV. Panel (b) is for χ^2 values as a function of L. The inset of panel (b) is the density dependence of symmetry energy with different L values.

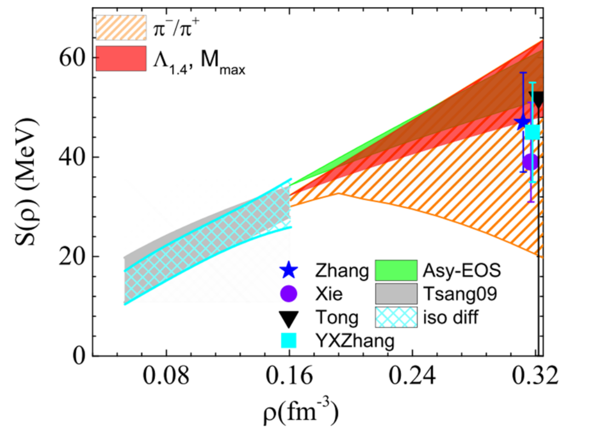

FIG. 9. Constraints of density dependence of the symmetry energy from π^-/π^+ in UrQMD (orange shaded region). Red solid region is the constraints from π^-/π^+, $\Lambda_{1.4}$, and $M_{\max}$ (see more details in the text).

To see the effects of density dependence of the symmetry energy on the $M(\pi)$ and π^-/π^+, we calculate central collisions for Au+Au with five kinds of density dependence of the symmetry energy, i.e., S_1, S_2, S_3, G_{05}, and G_{20}, as in Table II with $\sigma^{\text{OBEM}}_{N\Delta\to NN}(\sqrt{s}, m_\Delta)$ and $K_0 = 231$ MeV. The selected five forms of the symmetry energy include the uncertainties of the symmetry energy coefficient (S_0) and the slope of symmetry energy (L). All the results are plotted in Figs. 7(e) and 7(f). The lines with black color are the results obtained with G_{05} and G_{20}, and lines with red color are the results obtained with S_1, S_2, and S_3. As illustrated in bottom panels, $M(\pi)$ is not sensitive to the density dependence of symmetry energy, while the π^-/π^+ ratio is more sensitive to the stiffness of symmetry energy at 0.4A GeV.

D. Constraints on symmetry energy at high density

1. From π^-/π^+ ratio

As in many previous works, we tried to compare our calculations to the FOPI data and extract information of symmetry energy at one to two times normal density. Ideally, we should do χ^2 method properly to get the best values of L and S_0 and its uncertainties on the two-dimensional parameter space. But, considering both uncertainties of S_0 and L, one cannot obtain it with only five symmetry energy forms (S_1, S_2, S_3, G_{05}, G_{20}), as in Table II in the work.

In our following analysis, we only vary $L = 5$, 20, 35, 54, 70, 84, 100, 114, and 144 MeV and keep $S_0 = 32.5$ MeV. For $L = 54$–144 MeV, we adopt the power law form of $S(\rho)$. For $5 \leqslant L < 25$ MeV, the simple power law form of $S(\rho)$ will not valid since it gives an unreasonable symmetry energy at subnormal density. The $L < 5$ MeV sets are not adopted, because the corresponding symmetry energy becomes negative for densities above $2.7\rho_0$ and the EOS will not favor the neutron star. Thus, the Skyrme polynomial form of $S(\rho)$ are used in the calculations for $L = 5$, 20, and 35 MeV. For the given values of L, the parameters of A, B, and C in Eq. (3) are determined according to the relationship in Ref. [58] with $K_0 = 231$ MeV, $S_0 = 32.5$ MeV, $m^*/m = 0.77$, and $f_I = (m/m^*_n - m/m^*_p) = 0.0$.

In the left panel of Fig. 8, we present the π^-/π^+ ratios as a function of L at $S_0 = 32.5$ MeV. Our calculations show that π^-/π^+ monotonously decreases with L when $L > 50$ MeV, but the π^-/π^+ ratios are insensitive to L when $L < 50$ MeV. A possible reason is that the weak density dependence of symmetry energy at 1–2ρ_0, as shown in the inset of Fig. 8, leads to weak force from symmetry potential due to small $\frac{dV_{\text{sym}}}{d\rho}$ in the force calculations, i.e.,

$$F_{\text{sym}} = -\frac{dV_{\text{sym}}}{dr} = -\frac{dV_{\text{sym}}}{d\rho}\frac{d\rho}{dr}, \tag{10}$$

where V_{sym} is the symmetry potential. Consequently, the effect of symmetry energy on π^-/π^+ ratios becomes weak when $L = 5$–35 MeV and hard to distinguish by π^-/π^+ ratios. This behavior has been called the blind spots of probing the high-density symmetry energy with heavy ion collisions in Ref. [59]. In the right panel of Fig. 8, we plot the χ^2 as a function of L. We can only draw the conclusion $5 < L < 91$ MeV from the data of π^-/π^+ at 0.4A GeV.

Based on the comparisons of our calculations to the FOPI data at the beam energy of 0.4A GeV, we indirectly obtain the corresponding density dependence of the symmetry energy for cold nuclear matter, which is shown in Fig. 9. The orange shaded region is the constraint obtained from π^-/π^+ ratio in this work. The upper limitation is obtained within 1σ uncertainty for fitting π^-/π^+ data at 0.4A GeV. The lower limitation is roughly taken as $L = 5$ MeV, and we will further constrain it based on the neutron star properties. The light green region is the constraint from ASY-EOS flow data [60], which is a narrow band because the symmetry energy coefficient is fixed to $S_0 = 34$ MeV. The blue star, purple circle, and black triangle are the constraints of symmetry energy at $2\rho_0$ from neutron star analysis, $S(2\rho_0) = 47 \pm 10$ MeV [7], $39\pm^{12}_{8}$ MeV [8], and $\leqslant$53 MeV [11], respectively. The cyan shaded region and square are the constraint from the combination analysis of isospin diffusion data, neutron skin, and neutron stars [58] in five-dimensional parameter space, which predict $S(2\rho_0) = 35$–55 MeV. The gray shaded region is the constraints of symmetry energy at subsaturation density based on the heavy ion collision observables, such as isospin

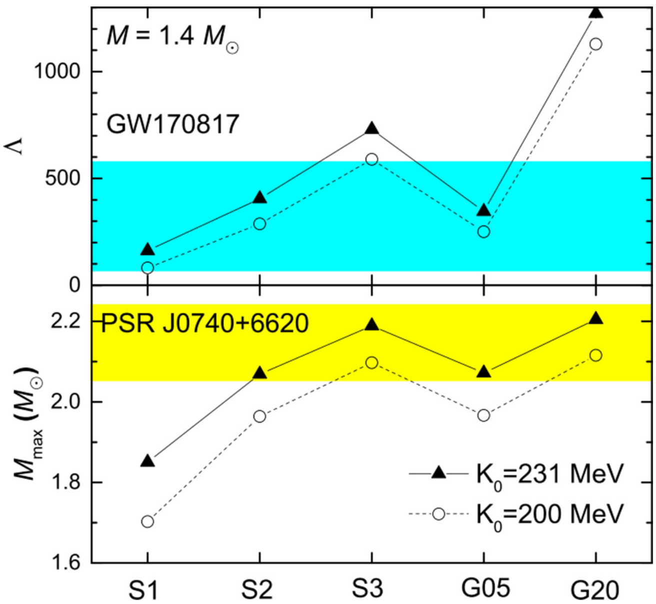

FIG. 10. Tidal deformability and maximum mass of neutron star obtained with the interaction we used in UrQMD model. The shaded regions are the constrained values of $\Lambda_{1.4}$ and $M_{\max}$ [2,70].

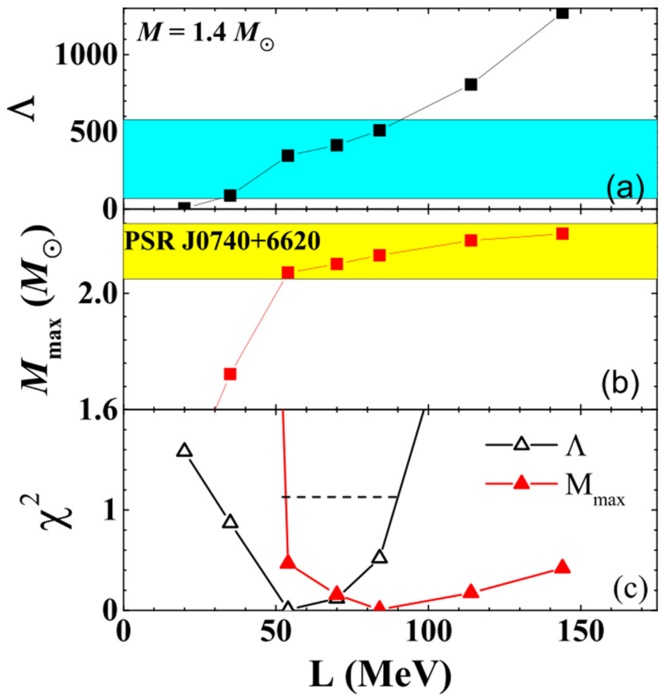

FIG. 11. (a) Λ as a function of L, (b) $M_{\max}$ as a function of L, and (c) χ^2 as a function of L for best fitting Λ (black open symbols) and $M_{\max}$ (red solid symbols).

diffusion and isospin transport ratio as a function of rapidity [58,61]. As observed in Fig. 9, the constraints on the symmetry energy at high density is consistent with the constraints from flow data and neutron stars, but with large uncertainties. One also should notice that the extracted values of L also depend on the value of S_0. A further χ^2 analysis on the S_0 and L plane is required, but it is beyond the scope of this work.

2. From neutron stars

By using the interactions used in this work, we calculate the equation of state (EoS) of neutron star matter in the density range $0.5\rho_0 < \rho < 3\rho_0$ which is obtained by simultaneously fulfilling the β stability and local charge neutrality conditions, including the contributions of e^- and μ^-. At subsaturation densities, the pasta phases of nuclear matter emerge, and we thus adopt the EoSs presented in Refs. [62–64] at $\rho < 0.08\ \mathrm{fm}^{-3}$. For the density region above $3\rho_0$, the UrQMD density functional does not apply and we adopt a polytropic EoS [9,65,66], where the pressure is given by $P = \kappa\rho^{\gamma'}$. At given γ', the parameter κ and energy density are fixed according to the continuity condition of pressure and baryon chemical potential at $\rho = 3\rho_0$. The structure of a neutron star is then obtained by solving the Tolman-Oppenheimer-Volkov equation, while the tidal deformability is estimated with $\Lambda = \frac{2k_2}{3}(\frac{R}{GM})^5$ [67–69]. In Fig. 10, we present the obtained tidal deformability at $M = 1.4\ M_\odot$ and the maximum mass based on those parameter sets we used. The solid symbols are the results obtained with $K_0 = 231$ MeV and open symbols are the results obtained with $K_0 = 200$ MeV. The shaded region is the constraints on Λ and $M_{\max}$ [2,70], obtained with the binary neutron star merger event GW170817 ($70 \leqslant \Lambda_{1.4} \leqslant 580$) [2] and the observational mass of PSR J0740+6620 ($2.14^{+0.10}_{-0.09}\ M_\odot$) [70] without violating the casuality limit ($\gamma' \leqslant 2.9$).

For the case of $K_0 = 200$ MeV, the symmetry energies of G_{20} and S_3 are required for describing the observational mass of PSR J0740+6620 ($2.14^{+0.09}_{-0.10}\ M_\odot$) [70] but cannot describe the data of Λ. Furthermore, the sets of G_{20} and S_3 have a large slope of symmetry energy and are not consistent with the recent commonly accepted L value [71–74]. If $K_0 = 231$ MeV are adopted in the calculations, we finally find that the parameter sets S_2 and G_{05} can reproduce $\Lambda_{1.4}$ and $M_{\max}$ simultaneously.

To get the constraints of L from the neutron star data, we present the results of Λ and $M_{\max}$ as a function of L, where L = 20, 35, 54, 70, 84, 100, 114, and 144 MeV in Figs. 11(a) and 11(b). In those calculations, we use the parameter set of $K_0 = 231$ MeV and $S_0 = 32.5$ MeV. The right panel of Fig. 11 presents the χ_i^2 as a function of L, and we obtain $L = 70^{+21}_{-16}$ MeV within 1σ uncertainties for fitting both $M_{\max}$ and Λ. The red solid region in Fig. 9 is the density dependence of the symmetry energy between $L = 54$ MeV and $L = 91$ MeV. At two times normal density, the $S(2\rho_0)$ is in 48–59 MeV. This value is consistent with those obtained from ASY-EOS flow [60] and neutron star analysis [7,8,11,58] within their uncertainties. The corresponding radius of a 1.4 solar mass neutron star is also obtained with $12.0 \leqslant R_{1.4} \leqslant 12.5$ km.

E. Remarks on $M(\pi)$ and π^-/π^+ in HICs

The other factors may also influence the prediction of $M(\pi)$ and π^-/π^+ to some extent, such as the momentum-dependent interaction [51], symmetry potential of $\Delta(1232)$

[29,30], the in-medium threshold effect [20], and the pion potential [26,28], and thus influence the exact values of the constrained symmetry energy. Those effects have been studied individually. In the following, we have short discussions on those effects, which indicate a weak influence on the our conclusion of symmetry energy constraints.

For example, the isospin-independent momentum-dependent interaction (MDI) also plays an important role on the $M(\pi)$ but less on π^-/π^+ ratios. In our previous discussions, the parameters of t_4 and t_5 in the MDI are determined by fitting $p+\mathrm{Ca}$ data of Arnold [75], which yields the effective mass $m^*/m = 0.77$ at Fermi momentum. After the analysis of a wealth of data by Hama [76], this form has been updated [77], which predicts a smaller effective mass. When we take $t_4 = 3.05$ MeV and $t_5 = 5 \times 10^{-4}$ MeV, the MDI can well reproduce Hama's data within $E_{\mathrm{inc}} = 0.7$ GeV and yield $m^*/m = 0.635$. With this updated MDI set, the UrQMD calculations show that the pion multiplicities are reduced by about 30%, while π^-/π^+ ratios are reduced by <1.5%. Thus, it indicates that the sensitivity of π^-/π^+ ratios on symmetry energy will not be dramatically changed by using two different forms of MDI.

For the symmetry potential of Δ, even its strength is not very clear; recent calculations [29,30] show that the standard Δ potential of Eq. (4) is a reasonable choice. When we artificially enhance the strength of Δ symmetry potential to two times that in Eq. (4), the calculations with UrQMD show negligible effect. It is consistent with the studies by Li [29], who showed that the total and differential π^-/π^+ ratio in heavy ion collisions above the threshold energy was weakly influenced by the completely unknown symmetry (isovector) potential of the $\Delta(1232)$ resonance, owing to the very short lifetimes of Δ resonances [29]. Although the results from the Tubingen QMD model have shown that the constraint of symmetry energy extracted from π^-/π^+ was highly sensitive to the strength of the isovector Δ potential [30], they also found that the standard Δ potential of Eq. (4) is suitable if the constrained L values are consistent with the results from nuclear structure and reaction studies.

Concerning the in-medium threshold effect, the relativistic Vlasov–Uehling–Uhlenbeck transport model (RVUU) model calculations show that the in-medium threshold effect enhances both the $M(\pi)$ and π^-/π^+ compared to those without considering this effect [20]. On the other hand, the calculations with the RVUU model show that including the pion potential decreases the π^-/π^+ ratio. Thus, a cancellation effect on the net π^-/π^+ ratio may take place when including both the threshold effect and pion potential in the calculations. To describe the experimental data, a softer symmetry energy with the slope parameter $L = 59$ MeV is needed in RVUU calculations [26]. The conclusion on the symmetry energy is consistent with our work.

Our calculations show that the different incompressibility, the momentum-dependent interaction, and symmetry potential of Δ in our selected values will not obviously change our conclusion on the symmetry energy. If we change MDI to the form with $m^*/m = 0.635$, there are still some difficulties for simultaneously describing the nucleonic flow, $M(\pi)$, and π^-/π ratios in the UrQMD model. It stimulates us to systematically study the influence of K_0, m^*/m, $(m_n^* - m_p^*)/m$, S_0, and L on HIC observables and extract their correlations based on the HIC data. It naturally requires more experimental data near the threshold energy and a Bayesian analysis in multidimensional parameter space.

IV. SUMMARY AND OUTLOOK

In the framework of the UrQMD model, we analyze the pion production mechanism at beam energies ranging from 0.4A to 1.0A GeV. We demonstrate again that the pions experience averaged 4.5 times more loops before freezing out. The loop of $N\pi \leftrightarrow \Delta$ and $NN \leftrightarrow N\Delta$ weaken the symmetry energy effect, especially at the beam energy above 0.6A GeV. Furthermore, we also analyze the characteristic density probed by pion multiplicities and its ratios, and we find that the pion observables probe the symmetry energy in 1–2.5 normal density for beam energies ranging from 0.4A to 1.0A GeV.

Considering the $\sigma^{\mathrm{OBEM}}_{N\Delta\to NN}(\sqrt{s}, m_\Delta)$, which takes into account the Δ-mass dependence of the $\mathcal{M}$ matrix and $p_{N\Delta}(m_\Delta)$, in the UrQMD model calculations, the values of $M(\pi)$ are obviously enhanced and π^-/π^+ ratios are suppressed a little bit, and both the $M(\pi)$ and π^-/π^+ ratios are close to the FOPI data. By investigating the influence of symmetry energy on the π^-/π^+ and comparing the calculations to the FOPI data, we find that the parameter sets with $5 < L < 91$ MeV can describe the data within the data uncertainties. Together with the constraints from neutron stars, such as $\Lambda_{1.4}$ and $M_{\max}$, we obtain $S(2\rho_0) = 48$–59 MeV and $L = 54$–91 MeV, which are consistent with the results from ASY-EOS flow data.

Furthermore, the model dependence is still an open question for precisely constraining the symmetry energy by comparing the data to the transport model calculations. For example, the momentum-dependent interaction, threshold effect, and pion potential are also important for the energy spectral of pion production and ratios at subthreshold energy, which should be figured out with the data of reaction $^{132,112,108}\mathrm{Sn} + {}^{124,112}\mathrm{Sn}$ [21]. Simultaneously describing the nucleonic flow and pion ratios observables could be a better way to reduce the uncertainties of the constraints on symmetry energy at one to two times normal density. For extracting the symmetry energy at density above $2.5\rho_0$ in the laboratory, our calculations show that we may need another probe, such as kaons or other new observables.

ACKNOWLEDGMENTS

This work was supported by the National Natural Science Foundation of China Grants No. 11790325, No. 11875323, No. 11875125, No. U2032145, No. 12047568, No. 11705163, No. 11790320, No. 11790323, and No. 11961141003; the National Key R&D Program of China under Grant No. 2018 YFA0404404; the Continuous Basic Scientific Research Project (No. WDJC-2019-13, No. BJ20002501); and the China Institute of Atomic Energy. Y.X.Z. thanks Prof. H. Wolter, M. B. Tsang, and A. Ono for the helpful discussions. The fruitful discussions with Jan Steinheimer are greatly appreciated. Q.L. also appreciates the support of the "Ten-Thousand Talent Program" of Zhejiang Province, the National Key Research and Development Program of China under Grant No. 2020YFE0202002. Y.C. also is thankful for the partial support of the Chinese-Polish Joint Project by National Science Foundation of China Grant No. 11961131010. We acknowledge support by the computing server C3S2 in Huzhou University.

[1] B. P. Abbott *et al.* (LIGO Scientific Collaboration and Virgo Collaboration), Phys. Rev. Lett. **119**, 161101 (2017).
[2] B. P. Abbott *et al.* (LIGO Scientific Collaboration and Virgo Collaboration), Phys. Rev. Lett. **121**, 161101 (2018).
[3] F. J. Fattoyev, J. Piekarewicz, and C. J. Horowitz, Phys. Rev. Lett. **120**, 172702 (2018).
[4] E. Annala, T. Gorda, A. Kurkela, and A. Vuorinen, Phys. Rev. Lett. **120**, 172703 (2018).
[5] B. P. Abbott *et al.* (LIGO Scientific Collaboration and Virgo Collaboration), Phys. Rev. X **9**, 011001 (2019).
[6] T. Malik, B. K. Agrawal, J. N. De, S. K. Samaddar, C. Providencia, C. Mondal, and T. K. Jha, Phys. Rev. C **99**, 052801(R) (2019).
[7] N. B. Zhang, B. A. Li, and J. Xu, Eur. Phys. J. A **55**, 39 (2019).
[8] W.-J. Xie and B.-An. Li, Astrophys. J. **883**, 174 (2019).
[9] C. Y. Tsang, M. B. Tsang, P. Danielewicz, W. G. Lynch, and F. J. Fattoyev, Phys. Lett. B **796**, 1 (2019).
[10] M. B. Tsang, W. G. Lynch, P. Danielewicz, and C. Y. Tsang, Phys. Lett. B **795**, 533 (2019).
[11] H. Tong, P. Zhao, and J. Meng, Phys. Rev. C **101**, 035802 (2020).
[12] J. Carlson, M. P. Carpenter, R. Casten, C. Elster, P. Fallon, A. Gade, C. Gross, G. Hagen, A. C. Hayes, D. W. Higinbotham *et al.*, Prog. Part. Nucl. Phys. **94**, 68 (2017).
[13] NuPECC Long Range Plan 2017, Perspectives for Nuclear Physics, http://www.nupecc.org/lrp2016/Documents/lrp2017.pdf.
[14] B. A. Li, Phys. Rev. Lett. **88**, 192701 (2002).
[15] B. A. Li, Nucl. Phys. A **708**, 365 (2002).
[16] W. Reisdorf, M. Stockmeier, A. Andronic, M. L. Benabderrahmane, O. N. Hartmann, N. Herrmann *et al.*, Nucl. Phys. A **781**, 459 (2007).
[17] Z. G. Xiao, B. A. Li, L. W. Chen, G. C. Yong, and M. Zhang, Phys. Rev. Lett. **102**, 062502 (2009).
[18] W. J. Xie, J. Su, L. Zhu, and F. S. Zhang, Phys. Lett. B **718**, 1510 (2013).
[19] Z. Q. Feng and G. M. Jin, Phys. Lett. B **683**, 140 (2010).
[20] T. Song and C. M. Ko, Phys. Rev. C **91**, 014901 (2015).
[21] G. Jhang, J. Estee, J. Barney, G. Cerizza, M. Kaneko, J. W. Lee, W. G. Lynch *et al.*, Phys. Lett. B **813**, 136016 (2021).
[22] G. Ferini, M. Colonna, T. Gaitanos, and M. D. Toro, Nucl. Phys. A **762**, 147 (2005).
[23] J. Xu, L.-W. Chen, C. M. Ko, B.-An. Li, and Yu.-G. Ma, Phys. Rev. C **87**, 067601 (2013).
[24] W.-M. Guo, G.-C. Yong, H. Liu, and W. Zuo, Phys. Rev. C **91**, 054616 (2015).
[25] M. Cozma, Phys. Rev. C **95**, 014601 (2017).
[26] Z. Zhang and C.-M. Ko, Phys. Rev. C **95**, 064604 (2017).
[27] Y. Y. Liu, Y. J. Wang, Q. F. Li, and L. Liu, Phys. Rev. C **97**, 034602 (2018).
[28] J. Hong and P. Danielewicz, Phys. Rev. C **90**, 024605 (2014).
[29] B.-An. Li, Phys. Rev. C **92**, 034603 (2015).
[30] M. Cozma, Phys. Lett. B **753**, 166 (2016).
[31] N. Ikeno, A. Ono, Y. Nara, and A. Ohnishi, Phys. Rev. C **93**, 044612 (2016).
[32] N. Ikeno, A. Ono, Y. Nara, and A. Ohnishi, Phys. Rev. C **101**, 034607 (2020).
[33] Z. Zhang and C. M. Ko, Phys. Rev. C **97**, 014610 (2018).
[34] E. E. Kolomeitsev, C. Hartnack, H. W. Barz *et al.*, J. Phys. G **31**, S741 (2005).
[35] J. Xu, L.-W. Chen, Man Yee Betty, H. Wolter, Y.-X. Zhang, J. Aichelin, M. Colonna, D. Cozma, P. Danielewicz, Z.-Q. Feng, A. Le Fevre, T. Gaitanos, C. Hartnack, K. Kim, Y. Kim, C.-M. Ko, B.-A. Li, Q.-F. Li, Z.-X. Li, P. Napolitani, A. Ono, M. Papa, T. Song, J. Su, J.-L. Tian, N. Wang, Y.-J. Wang, J. Weil, W.-J. Xie, F.-S. Zhang, and G.-Q. Zhang, Phys. Rev. C **93**, 044609 (2016).
[36] Y.-X. Zhang, Y.-J. Wang, M. Colonna, P. Danielewicz, A. Ono, M. B. Tsang, H. Wolter, J. Xu, L.-W. Chen, D. Cozma, Z. Q. Feng, S. Das Gupta, N. Ikeno, C. M. Ko, B. A. Li, Q. F. Li, Z. X. Li, S. Mallik, Y. Nara, T. Ogawa, A. Ohnishi, D. Oliinychenko, M. Papa, H. Petersen, J. Su, T. Song, J. Weil, N. Wang, F. S. Zhang, and Z. Zhang, Phys. Rev. C **97**, 034625 (2018).
[37] A. Ono, J. Xu, M. Colonna, P. Danielewicz, C. M. Ko, M. B. Tsang, Y.-J. Wang, H. Wolter, Y.-X. Zhang, L.-W. Chen, D. Cozma, H. Elfner, Z. Q. Feng, N. Ikeno, B. A. Li, S. Mallik, Y. Nara, T. Ogawa, A. Ohnishi, D. Oliinychenko, J. Su, T. Song, F. S. Zhang, and Z. Zhang, Phys. Rev. C **100**, 044617 (2019).
[38] S. A. Bass, M. Belkacem, M. Bleicher, M. Brandstetter, L. Bravina, C. Ernst, L. Gerland, M. Hofmann, S. Hofmann, J. Konopka, G. Mao, L. Neise, S. Soff, C. Spieles, H. Weber, L. A. Winckelmann, H. Stöcker, and W. Greiner, Prog. Part. Nucl. Phys. **41**, 255 (1998).
[39] Q. F. Li, Z. X. Li, S. Soff, M. Bleicher, and H. Stöcker, Phys. Rev. C **72**, 034613 (2005).
[40] Q. F. Li, C. W. Shen, C. C. Guo, Y. J. Wang, Z. X. Li, J. Lukasik, and W. Trautmann, Phys. Rev. C **83**, 044617 (2011).
[41] Y. Nara, N. Otuka, A. Ohnishi, K. Niita, and S. Chiba, Phys. Rev. C **61**, 024901 (1999).
[42] J. Weil, V. Steinberg, J. Staudenmaier, L. G. Pang, D. Oliinychenko, J. Mohs, M. Kretz, T. Kehrenberg, A. Goldschmidt, B. Bauchle *et al.*, Phys. Rev. C **94**, 054905 (2016).
[43] Y. Zhang, N. Wang, Q. Li, Li. Ou, J. Tian, M. Liu, K. Zhao, X. Wu, and Z. Li, Fron. Phys. **15**, 54301 (2020).
[44] J. Aichelin, A. Rosenhauer, G. Peilert, H. Stoecker, and W. Greiner, Phys. Rev. Lett. **58**, 1926 (1987).
[45] Y. Wang, C. Guo, Q. Li, A. Le Fevred, Y. Leifels, and W. Trautmann, Phys. Lett. B **778**, 207 (2018).
[46] S. Shlomo *et al.*, Eur. Phys. J. A **30**, 23 (2006).
[47] Y. Ye, Y. Wang, J. Steinheimer, Y. Nara, H.-jie Xu, P. Li, D. Lu, Q. Li, and H. Stoecker, Phys. Rev. C **98**, 054620 (2018).
[48] V. Flaminio, W. G. Moorhead, D. R. O. Morrison, and N. Rivoire, CERN Report No. CERN-HERA-8401, Geneva, Switzerland, 1984 (unpublished).
[49] P. Danielwicz and G. Bertsch, Nucl. Phys. A **533**, 712 (1991).

[50] Y. Cui, Y. X. Zhang, and Z. X. Li, Chin. Phys. C **44**, 024106 (2020).
[51] Q. F. Li, Z. X. Li, S. Soff, M. Bleicher, and H. Stöcker, J. Phys. G: Nucl. Part. Phys. **32**, 151 (2006).
[52] S. A. Bass, C. Hartnack, H. Stöker, and W. Greiner, Phys. Rev. C **51**, 3343 (1995).
[53] H.-L. Liu, G.-C. Yong, and D.-H. Wen, Phys. Rev. C **91**, 044609 (2015).
[54] A. Le Fevre, Y. Leifels, W. Reisdorf, J. Aichelin, and C. Hartnack, Nucl. Phys. A **945**, 112 (2016).
[55] C. Fuchs, Prog. Part. Nucl. Phys. **56**, 1 (2006).
[56] Q. F. Li, Z. X. Li, S. Soff, R. Gupta, M. Bleicher, and H. Stöcker, J. Phys. G: Nucl. Part. Phys. **31**, 1359 (2005).
[57] Q. F. Li, Z. X. Li, E. Zhao, and R. K. Gupta, Phys. Rev. C **71**, 054907 (2005).
[58] Y. Zhang, M. Liu, C. Xia, Z. Li, and S. K. Biswal, Phys. Rev. C **101**, 034303 (2020).
[59] G.-C. Yong, Phys. Lett. B **786**, 422 (2018).
[60] P. Russotto, S. Gannon, S. Kupny, P. Lasko, L. Acosta, M. Adamczyk, A. Al-Ajlan, M. Al-Garawi, S. Al-Homaidhi, F. Amorini *et al.*, Phys. Rev. C **94**, 034608 (2016).
[61] M. B. Tsang, Y. Zhang, P. Danielewicz, M. Famiano, Z. Li, W. G. Lynch, and A. W. Steiner, Phys. Rev. Lett. **102**, 122701 (2009).
[62] R. P. Feynman, N. Metropolis, and E. Teller, Phys. Rev. **75**, 1561 (1949).
[63] G. Baym, C. Pethick, and P. Sutherland, Astrophys. J. **170**, 299 (1971).
[64] J. W. Negele and D. Vautherin, Nucl. Phys. A **207**, 298 (1973).
[65] J. M. Lattimer and M. Prakash, Phys. Rep. **621**, 127 (2016).
[66] F. J. Fattoyev, J. Carvajal, W. G. Newton, and B.-A. Li, Phys. Rev. C **87**, 015806 (2013).
[67] T. Damour and A. Nagar, Phys. Rev. D **80**, 084035 (2009).
[68] T. Hinderer, B. D. Lackey, R. N. Lang, and J. S. Read, Phys. Rev. D **81**, 123016 (2010).
[69] S. Postnikov, M. Prakash, and J. M. Lattimer, Phys. Rev. D **82**, 024016 (2010).
[70] H. T. Cromartie, E. Fonseca, S. M. Ransom, P. B. Demorest, Z. Arzoumanian, H. Blumer, P. R. Brook, M. E. De Cesar, T. Dolch, J. A. Ellis *et al.*, Nat. Astron. **4**, 72 (2020).
[71] J. M. Lattimer and A. W. Steiner, Eur. Phys. J. A **50**, 40 (2014).
[72] B.-An. Li and X. Han, Phys. Lett. B **727**, 276 (2013).
[73] M. B. Tsang, J. R. Stone, F. Camera, P. Danielewicz, S. Gandolfi, K. Hebeler, C. J. Horowitz, J. Lee, W. G. Lynch *et al.*, Phys. Rev. C **86**, 015803 (2012).
[74] Y. Zhang, J. Tian, W. Cheng, F. Guan, Y. Huang, H. Li, L. Lu, R. Wang *et al.*, Phys. Rev. C **95**, 041602(R) (2017).
[75] L. G. Arnold *et al.*, Phys. Rev. C **25**, 936 (1982).
[76] S. Hama, B. C. Clark, E. D. Cooper, H. S. Sherif, and R. L. Mercer, Phys. Rev. C **41**, 2737 (1990).
[77] C. Hartnack and J. Aichelin, Phys. Rev. C **49**, 2801 (1994).